MATERIALS SCIENCE

Large negative thermo-optic coefficients of a lead halide perovskite

Taketo Handa, Hirokazu Tahara, Tomoko Aharen, Yoshihiko Kanemitsu*

Lead halide perovskites are promising semiconductors for high-performance photonic devices. Because the refractive index determines the optimal design and performance limit of the semiconductor devices, the refractive index and its change upon external modulations are the most critical properties for advanced photonic applications. Here, we report that the refractive index of halide perovskite $CH_3NH_3PbCl_3$ shows a distinct decrease with increasing temperature, i.e., a large negative thermo-optic coefficient, which is opposite to those of conventional inorganic semiconductors. By using this negative coefficient, we demonstrate the compensation of thermally induced optical phase shifts occurring in conventional semiconductors. Furthermore, we observe a large and slow refractive index change in $CH_3NH_3PbCl_3$ during photoirradiation and clarify its origin to be a very low thermal conductivity supported by theoretical analysis. The giant thermo-optic response of $CH_3NH_3PbCl_3$ facilitates efficient phase modulation of visible light.

INTRODUCTION

Lead halide perovskites have attracted considerable attention in the fields of photonics and optoelectronics (*1*, *2*) owing to a combination of facile processability and exceptional optoelectronic properties, namely, large absorption coefficients (*3*), high photoluminescence (PL) quantum efficiencies (*4*), and long lifetime and diffusion length of photocarriers (*5*, *6*). These features have already led to astonishingly efficient solar cells (*7*), x-ray and gamma-ray detectors (*8*, *9*), light-emitting diodes (*10*), and lasers based on halide perovskites (*11*). Under actual operation conditions, these perovskite-based photonic devices will experience an unavoidable heating. To maintain high device performance under various thermal conditions, it is required to understand their thermophysical properties.

The temperature dependence of the refractive index is of particular importance for advanced photonic devices because many optical phenomena are governed by this optical constant, and this constant determines the optimal design and performance limit of photonic devices. The refractive indices of most commonly used photonic semiconductors (Si or GaAs) are known to increase as the temperature increases, namely, positive thermo-optic coefficient (*12*). Under any operation conditions, part of the provided power is inevitably dissipated as heat, resulting in a rise in lattice temperature. This induces refractive index changes and brings about detrimental impacts on the device performance. The understanding of the thermo-optic properties opens ways to suppress or compensate the thermally induced performance change (*13*). Therefore, the clarification of the thermo-optic responses of halide perovskites is crucial for future photonic applications and best possible utilization of their superior optoelectronic properties.

In this work, we investigate steady-state and transient thermo-optic responses of the halide perovskite $MAPbCl_3$ (MA = CH_3NH_3), and by using the unusual thermo-optic properties of the material, we demonstrate new applications of halide perovskites. We found that $MAPbCl_3$ has a negative thermo-optic coefficient with a large magnitude. By using this negative coefficient, we demonstrate the compensation of the temperature-induced optical phase shift in inorganic semiconductors. We further investigate the transient refractive index change during photoinduced lattice heating with high-sensitivity interferometric techniques and show that a strong and slow thermo-optic response exists even under weak excitation. Our theoretical analysis clarifies that the transient response is determined by a very low thermal conductivity. The thermo-optic response of $MAPbCl_3$ is much stronger than that of other semiconductors, leading to efficient photoinduced phase modulation of visible light. The observed unconventional thermo-optic features are very similar to those in organic polymers or even liquids, indicative of the organic nature of halide perovskites in terms of thermophysical properties, providing new functionalities of halide perovskites.

RESULTS AND DISCUSSION

First, we show that our samples have high quality. The $MAPbCl_3$ single crystals with millimeter size were fabricated by using an antisolvent vapor–assisted crystallization method (Fig. 1A) (*14*). The high quality of the prepared sample was well supported by the x-ray diffraction pattern (fig. S1) and the transmission spectrum shown in Fig. 1B (red circles). The transmittance exhibits a steep onset at 425 nm and reaches a value as high as 80% for longer wavelengths. The measured spectrum agrees well with the transmittance curve obtained using the Fresnel equation and the refractive index that is experimentally determined by independent measurements (see fig. S2 and the Supplementary Materials). This shows that our sample has negligible scattering losses and a high transparency in the visible region, which is very important for photonic device applications.

Using the obtained high-quality $MAPbCl_3$ crystal, we determined the refractive indices at different temperatures by measuring the incident angle dependence of the surface reflectance (see Materials and Methods and fig. S2). The top panel of Fig. 1C shows the refractive indices measured at various wavelengths and temperatures between 198 and 323 K, where $MAPbCl_3$ is in the cubic phase (*15*). We confirmed that the refractive indices at 298 K are in good agreement with the reported values determined by ellipsometry at room temperature (*16*). The bottom panel of Fig. 1C shows the thermo-optic coefficient, dn/dT, obtained by fitting the temperature dependence of the refractive index with a linear function (see fig. S3). These data reveal that $MAPbCl_3$ has a negative thermo-optic coefficient with a large magnitude. The coefficient is -3.0×10^{-4} /K at 430 nm, and this is close to that of CCl_4 (-5.9×10^{-4} /K) (*17*), a liquid with a highly temperature-responsive

Institute for Chemical Research, Kyoto University, Uji, Kyoto 611-0011, Japan.
*Corresponding author. Email: kanemitu@scl.kyoto-u.ac.jp

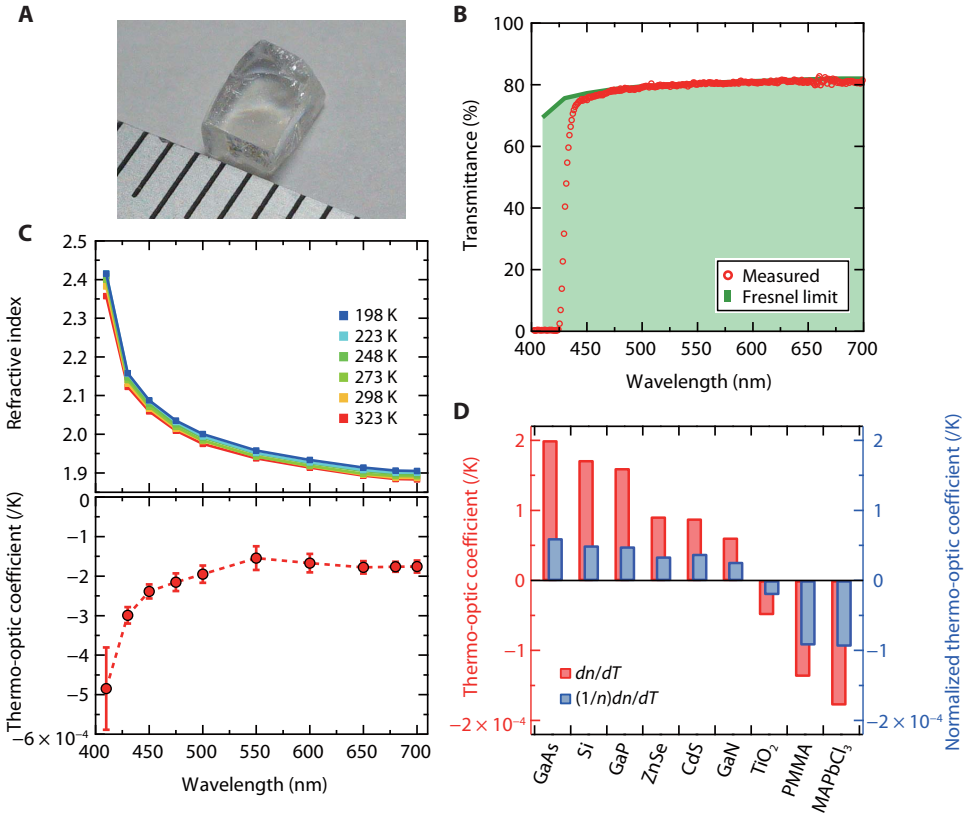

Fig. 1. Large negative thermo-optic coefficient of $MAPbCl_3$. (**A**) Photograph of the $MAPbCl_3$ single crystal. The scale interval is 1 mm. (**B**) Transmission spectrum of the $MAPbCl_3$ single crystal. Green-shaded area shows the transmittance in the Fresnel limit calculated from the refractive index of $MAPbCl_3$. (**C**) Refractive indices between 198 and 323 K (top) and thermo-optic coefficient of $MAPbCl_3$ (bottom). (**D**) Thermo-optic coefficient of $MAPbCl_3$ compared with those of other materials. PMMA, poly(methyl methacrylate). The coefficients of the different materials were measured at different wavelengths, which are summarized in table S1. Photo credit: Taketo Handa, Kyoto University.

refractive index used for high-sensitivity photothermal deflection spectroscopy. In Fig. 1D, the thermo-optic coefficient of $MAPbCl_3$ is compared with the reported coefficients of other materials including conventional inorganic semiconductors and an organic polymer. The coefficients used in this figure are summarized in table S1. The comparison demonstrates that the negative thermo-optic coefficient with large magnitude of $MAPbCl_3$ is unusual when considering its superior inorganic-like optoelectronic responses.

Motivated by the discovery of the negative thermo-optic coefficient of $MAPbCl_3$, we design a system to compensate the optical phase shift occurring in conventional inorganic semiconductors. Thermal effects including the positive refractive index change and thermal expansion in conventional semiconductors are known to alter photonic device properties, such as optical phase shifts or resonant frequency drifts (*13*). The large negative thermo-optic coefficient of $MAPbCl_3$ will, thus, serve to compensate these thermal effects. To demonstrate this, we constructed a Mach-Zehnder–type interferometer (Fig. 2A) and performed the compensation of the thermally induced phase shift in a conventional semiconductor (ZnSe) by using an additional $MAPbCl_3$ crystal. ZnSe was selected for this examination because it has a positive and relatively large thermo-optic coefficient (Fig. 1D). To monitor the optical phase, a broadband white light was used as a light source and split into a probe beam with vertical polarization and a reference beam with horizontal polarization. In the probe path, the ZnSe sample was mounted on a cold finger of an evacuated cryostat, while another ZnSe sample with the same thickness was placed in the reference path under ambient air. The optical path length within the sample in the cryostat was altered by changing the sample temperature, which leads to the optical phase shift given by

$$\Delta\phi = -\frac{2\pi L}{\lambda}\left(\frac{dn}{dT} + n\frac{1}{L}\frac{dL}{dT}\right)\Delta T \quad (1)$$

where L is the thickness of the material that the light passes, λ is the wavelength of the light, dn/dT is the thermo-optic coefficient, and $(1/L)dL/dT$ is the linear thermal expansion coefficient (see the Supplementary Materials for details). For most inorganic semiconductors and also for $MAPbCl_3$, the contribution of the thermal expansion is smaller than that of the thermo-optic coefficient (fig. S4). By monitoring the interference intensity between the probe and reference beams, the temperature-induced phase shift can be determined with high sensitivity.

Figure 2B shows the interference intensity map for a 3-mm-thick ZnSe crystal without the $MAPbCl_3$ crystal. The periodic intensity change observed along the vertical axis is a result of the temperature-dependent phase shift within the ZnSe crystal in the cryostat. In Fig. 2C, we show the temperature dependence of the interference intensity and the corresponding phase shift at 753 nm. This result shows that even small changes in temperature cause the large optical phase shifts due

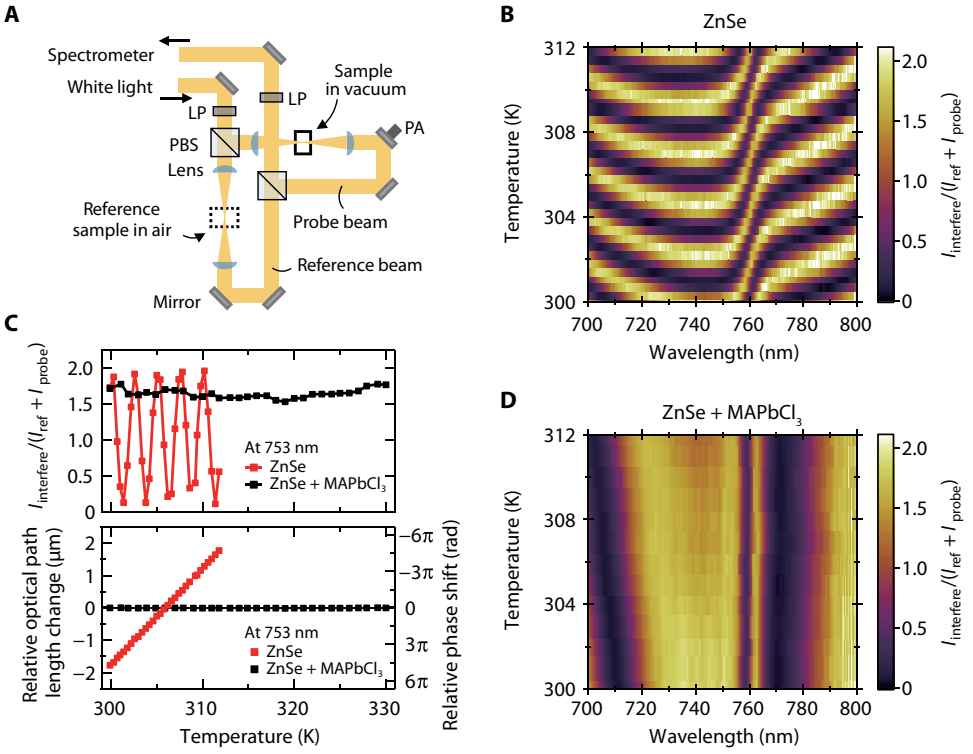

Fig. 2. Compensation of thermally induced phase shift in an inorganic semiconductor using $MAPbCl_3$. (**A**) Schematic illustration of the modified Mach-Zehnder interferometer. PBS, polarizing beam splitter; LP, linear polarizer whose angle is set to 45° with respect to the horizontal axis of the PBS; PA, piezoelectric actuator. The temperature of the sample in the probe path can be controlled. (**B**) Interference intensity map upon changing the temperature of the ZnSe crystal in the probe path. The map is normalized by the sum of reference and probe spectra. The spectral shape of the peak-valley structure at 300 K originates from the chirps of the probe and reference beams. (**C**) Temperature dependences of the interference intensity (top) and relative optical path length change and phase shift (bottom) at 753 nm. (**D**) Compensation of the optical phase shift in (B) by using the $MAPbCl_3$ crystal.

to the increase of the optical path length in the ZnSe crystal. In comparison, the optical phase shift is drastically suppressed by additionally placing a 3.9-mm-thick $MAPbCl_3$ single crystal in front of the ZnSe crystal (Fig. 2D). In particular, at 753 nm, the interference intensity is independent of the temperature in the range of 30 K around room temperature, i.e., the thermal effects in ZnSe are fully compensated (Fig. 2C). The wavelength resulting in the full compensation can be controlled by simply changing the thickness of the $MAPbCl_3$ crystal. The wide bandgap and high transparency of $MAPbCl_3$ are useful for realizing the phase-shift compensation of light in the visible and near-infrared regions. The facile processability of halide perovskites coupled with the large negative thermo-optic coefficient offers solutions to the thermally induced issues in photonic applications.

The observed large magnitude of the thermo-optic coefficient indicates that local heat generation during actual device operation (e.g., nonradiative photocarrier recombination or Joule heating) will cause the large refractive index change of active perovskite layer. We investigated the refractive index change during optical excitation because this is a particularly important operational condition for lasers, photodetectors, and solar cells. Furthermore, to clarify the lattice heating mechanism, we studied the temporal thermo-optic response by combining the Mach-Zehnder interferometer with a pump beam–synchronized data acquisition system (fig. S5) (*18*). A femtosecond-pulsed laser operating at 750 nm (repetition rate of 200 kHz) was used as a pump pulse. The pump laser was modulated at 4 Hz by an optical chopper, which periodically generates carriers via two-photon absorption and serves as a heat source through hot-carrier relaxation and nonradiative recombination. Under this excitation condition, we observed a blue PL emission (fig. S6) and confirmed that carriers are actually generated. The PL spectral shape is in agreement with the transmission edge of the crystal due to strong reabsorption effect (*19*). The weak absorption under two-photon excitation enables a large optical penetration depth along the optical axis (fig. S7).

Figure 3A shows the temporal change of the interference intensity between the 650-nm probe and reference beams, where the probe beam has passed through a 3.75-mm-thick $MAPbCl_3$ crystal excited by the 750-nm pump light with the power of 33 mW. The vertical axis data were obtained by changing the probe path length on the order of nanometer with a piezoelectric actuator. We estimate an effective carrier density of 4.1×10^{15} cm^{-3} from the two-photon absorption coefficient $\beta = 2.43$ cm/GW at 750 nm, and a spot size of 68.4 μm and a pulse duration of 230 fs for the pump pulse (see Materials and Methods). This moderate carrier density implies almost no Auger heating for this excitation density. The corresponding steady-state absorbed power density is 2.4 kW/cm^3, which is similar to the 1 sun solar irradiation condition and much weaker than laser operation condition (see the Supplementary Materials). The optical phase shift at the time of 250 ms, i.e., 125 ms after the irradiation start, is shown with the green line in Fig. 3B and reveals a large shift of ~π even under this weak excitation condition. The positive phase shift corresponds to a shortening of the optical path length because of the pump beam–induced lattice heating. This positive shift is in agreement with the negative thermo-optic coefficient of

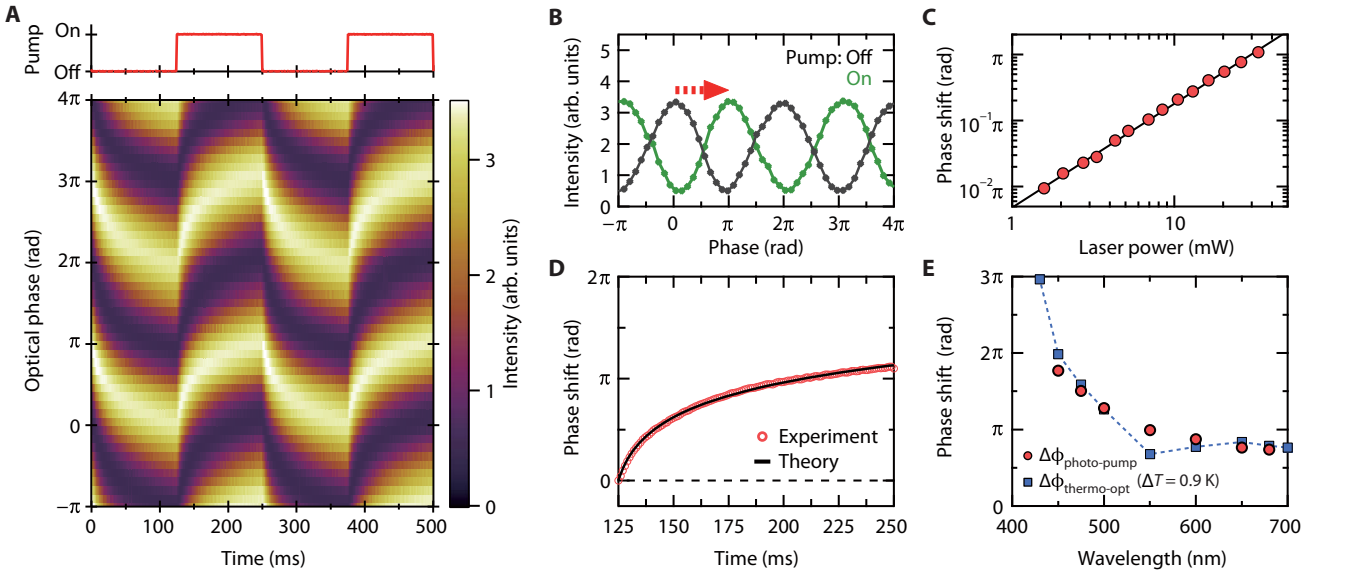

Fig. 3. Photoinduced lattice heating and dynamic thermo-optic phase shift in $MAPbCl_3$. (**A**) Contour plot of interference intensity between the 650-nm probe and reference beams (bottom) for periodic irradiation of $MAPbCl_3$ by the 750-nm pump light with a power of 33 mW (top). (**B**) Interference intensity at times of 125 ms (black data; without pump illumination) and 250 ms (green data; with pump illumination). (**C**) Optical phase shift as a function of the pump beam power. (**D**) Temporal evolution of the phase shift extracted from (A). The solid line shows the fitting result. (**E**) Probe-wavelength dependence of the phase shift under excitation with 26 mW (red circles) and the shift predicted from Eq. 1 with the estimated temperature rise of 0.9 K (blue squares).

$MAPbCl_3$. In Fig. 3C, we provide the pump power dependence of the phase shift. The result shows that the phase shift exhibits a power law with an exponent of 1.57, and the phase can be conveniently controlled by changing the pump power. We note that, under ideal conditions, a square dependence would be expected for two-photon excitation. The fact that the exponent is less than 2 is considered to be a result of an excitation fluence–dependent nonradiative process (see the Supplementary Materials).

The origin of the large phase shift can be clarified by analyzing the transient of the photoinduced phase shift (Fig. 3D). The response is found to be very slow, on the order of tens of milliseconds. This is significantly slower than the pulse duration of the pump beam (230 fs) and lifetime of photocarriers (<1 ns confirmed by time-resolved PL measurements), thus the optical Kerr and band-filling effects can be excluded as the origin of the observed phase shift (*20*, *21*). The following theoretical analysis supports that the observed phase shift is governed by the photoinduced temperature rise and the intrinsic low heat conduction of $MAPbCl_3$. The temperature rise $\Delta T(r, t)$ at the position r and time t upon illuminating a solid by a Gaussian beam, starting illumination at $t = 0$, is expressed by (*22*)

$$\Delta T(r,t) = \frac{\eta_{heat} P_{abs}}{4\pi\kappa L}\left[\mathrm{Ei}\left(-\frac{r^2}{w_{pump}^2}\right) - \mathrm{Ei}\left(-\frac{r^2}{w_{pump}^2 + 4Dt}\right)\right] \quad (2)$$

where L is the sample thickness, w_{pump} is the radius of the Gaussian beam (the size defined by the $1/e$ radius of the intensity profile), and r represents the distance from the beam center. The term P_{abs} is the power absorbed by the material, and η_{heat} is the efficiency of the conversion of absorbed power into power that is actually used to heat the sample. The thermal diffusivity D can be expressed in terms of the thermal conductivity κ, the density ρ, and the specific heat capacity C_p; $D = \kappa/\rho C_p$. The exponential integral function $(-\int_{-z}^{\infty} e^{-s} s^{-1} ds)$ is denoted by $\mathrm{Ei}(z)$. For the present two-photon excitation, the absorbed power is given by $P_{abs} = \frac{(1-R)\beta I L P_{in}}{1+\beta I L}$, where $R = 0.1$ is the reflectivity at 750 nm and I and P_{in} are the peak irradiance and incident power of the 750-nm pump laser, respectively.

The fitting result shown in Fig. 3D with the solid line describes that the experimental result is well interpreted with the model based on the thermal conduction. From the numerical fitting of the transient phase shift based on Eqs. 1 and 2, we obtained 0.34 and 0.46 W/(m·K) for η_{heat} and κ, respectively (see the Supplementary Materials for details of the fitting procedure). The value of 0.34 for η_{heat} is reasonable when considering the high internal luminescence efficiency of halide perovskites, as explained in the Supplementary Materials (*23*). The obtained value of $\kappa = 0.46$ W/(m·K) for $MAPbCl_3$ is in good agreement with recent experimental works on $MAPbCl_3$ and slightly larger than that for $MAPbI_3$ [$\kappa \sim 0.3$ W/(m·K)] and for $MAPbBr_3$ [$\kappa \sim 0.4$ W/(m·K)] (*24*–*28*). Note that the thermal conductivity $\kappa = 0.46$ W/(m·K) for $MAPbCl_3$ is much lower than those of conventional inorganic semiconductors, but rather similar to those observed in an organic polymer or liquid (table S1). This observed low thermal conductivity is consistent with a recent theoretical study that suggests short phonon lifetimes in halide perovskites driven by enhanced phonon-phonon scattering (*29*). Furthermore, it is indicated that efficient local heating should occur upon heat generation inside the perovskite crystal due to the low κ. From Eq. 2 and the fitting results for η_{heat} and κ, we can derive an effective temperature rise of $\Delta T = 1.2$ K after the 125 ms of the pump irradiation (see fig. S8). We separately examined if the theoretically predicted temperature rise, coupled with Eq. 1, reproduces the experimentally observed photoinduced phase shift. Specifically, we measured the probe-wavelength dependence of the pump-induced phase shift for a pump power of 26 mW (red circles in Fig. 3E) and found a good agreement between the obtained shift and the shift derived from Eq. 1 and $\Delta T = 0.9$ K for 26 mW (blue squares in Fig. 3E). These results conclusively demonstrate that the thermo-optic response of $MAPbCl_3$ governs the large photoinduced phase shift of the visible light.

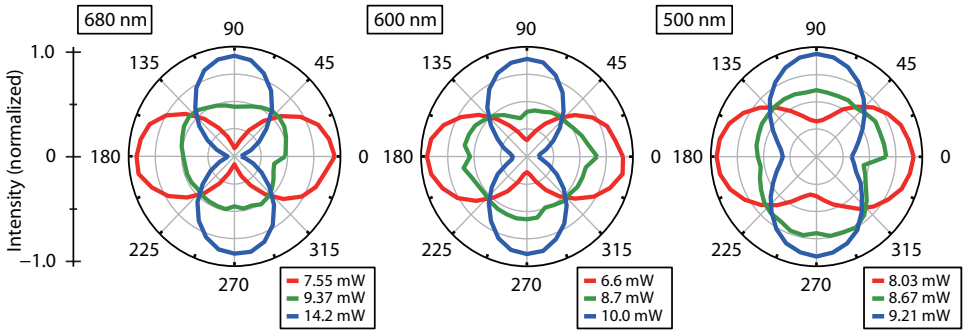

Fig. 4. Polarization control of visible light by using the thermo-optic response in $MAPbCl_3$. By changing the pump beam power as indicated, the optical phase of the probe light, which passes through the $MAPbCl_3$ crystal, is altered and thus the relative phase difference between the optical phases of probe and reference beams can be controlled.

The findings described above show that a temperature rise of ~1 K occurs within 100 ms even under weak excitation conditions due to the very low thermal conductivity of $MAPbCl_3$, and this rise modulates the optical phase largely. Figure S9 shows the comparison between the expected thermo-optic responses for $MAPbCl_3$ and other materials in the case of P_{abs} = 20 mW. The comparison shows that the thermo-optic response of $MAPbCl_3$ is much larger than the responses of conventional inorganic semiconductors. This fact indicates that the observed large phase shift during photoexcitation is very unique for $MAPbCl_3$. In other words, the giant thermo-optic response of $MAPbCl_3$ is applicable to achieve a highly efficient optical modulator in the visible range. In Fig. 4, we demonstrate that polarization of light can be controlled by manipulating the phase shift within the perovskite crystal. This polarization control (linear, circular, and cross-linear) is simply achieved by changing the pump beam power. The wide bandgap of $MAPbCl_3$ enables broadband optical modulation covering nearly the entire visible region. The revealed large negative thermo-optic coefficient and low thermal conductivity, featuring the thermophysical responses of organic materials or liquids, provide new thermo-optic functionality to halide perovskites.

MATERIALS AND METHODS

Synthesis and structural characterization of $MAPbCl_3$ single crystals

The $MAPbCl_3$ single crystals were grown using the antisolvent vapor–assisted crystallization method (*14*). The equimolar starting materials, MACl (Tokyo Chemical Industry Co. Ltd.) and $PbCl_2$ (Sigma-Aldrich), were first dissolved in dimethyl sulfoxide (FUJIFILM Wako Pure Chemical Corporation) to yield a perovskite solution with a concentration of 1 M. Then, the solution was diluted to a 0.5 M perovskite solution by adding *N*,*N*-dimethylformamide (Tokyo Chemical Industry Co. Ltd.). A small vial without lid and partially filled with the perovskite solution was loaded into a bigger vial containing toluene (antisolvent) so that the smaller vial is bathing in toluene. The lid of the bigger vial was closed tightly, and the vapor diffusion resulted in growth of large $MAPbCl_3$ single crystals. The x-ray diffraction pattern obtained from a cleaved $MAPbCl_3$ single crystal is provided in fig. S1. The sharp peaks verify a good crystal quality.

Incident angle dependence of surface reflection

The refractive index of $MAPbCl_3$, n_{MAPbCl_3}, was determined by the incident angle dependence of the surface reflectance and using Fresnel equations (*30*). The single crystal sample was attached to the cold finger of an evacuated cryostat (<10^{-5} torr) using silver paste. The reflectivity was measured using a tunable monochromatic optical beam obtained from a supercontinuum light source with a repetition rate of 40 MHz (SC-400-4, Fianium) and a monochromator (CT-25C, JASCO). The polarization of the light was set parallel to the plane of incidence (p-polarization) by a linear polarizer. The light was incident on the (001) surface of $MAPbCl_3$ with the incident angle θ. The reflected beam intensity at the reflection angle θ was measured by a laser power meter (PD300-3W and NOVA II, Ophir). The influence of the cryostat window was calibrated by performing the same measurement for a silicon wafer. The obtained reflectance under vacuum condition (n_{vacuum} = 1) was fitted by using the Fresnel equation for the reflectance of the p-polarized light (*30*)

$$R(\theta) = \left(\frac{\sqrt{1 - \left(\frac{\sin\theta}{n_{MAPbCl_3}}\right)^2} - n_{MAPbCl_3}\cos\theta}{\sqrt{1 - \left(\frac{\sin\theta}{n_{MAPbCl_3}}\right)^2} + n_{MAPbCl_3}\cos\theta} \right)^2 \quad (3)$$

The fitting was performed for angles ranging from θ = 40° to 70°. The temperature of the sample was controlled by using the liquid-He flow and a heater.

Mach-Zehnder interferometer for measuring the thermally induced optical phase shift

The Mach-Zehnder–type interferometer depicted in Fig. 2A was used for the measurements. As the light source to measure the optical phase shift, the picosecond pulsed white light from a supercontinuum light source (40 MHz; SC-400-4-PP, Fianium) was used. The white light first passed through long-pass and short-pass filters with cutoff wavelengths of 475 and 875 nm and then through a linear polarizer, whose angle was set to 45° with respect to the horizontal axis of a broadband polarizing beam splitter (PBS). The PBS splits the white light into two optical beams, namely, the reference beam with horizontal polarization and the probe beam with vertical polarization. We used the same kind of optics in both paths to obtain the same spectrum and suppress the difference between the optical chirps of the two paths. To obtain the interference pattern after the second PBS, both optical path lengths were adjusted to the same value under the condition T = 300 K by using an optical delay stage and a piezoelectric actuator and controller (PAS005 and MDT694B, Thorlabs), which control the path length on

the order of ~μm and ~nm, respectively. To verify the phase-shift compensation, we first measured the phase shift for a ZnSe crystal (3 mm thick, Edmund Optics) with a positive thermo-optic coefficient. The ZnSe crystal was positioned in the probe path by mounting it on a cold finger of an evacuated cryostat. Another ZnSe crystal with the same thickness as that in the probe path was placed in the reference path under ambient air. These ZnSe samples were obtained by cleaving one sample into two pieces with same thickness. The beam power at the sample position was 97 μW. We measured the spectral shape of the interference intensity using a spectrometer (USB2000, Ocean Optics) as a function of the sample temperature in the probe path and obtained the interference intensity in Fig. 2B. By using the piezoelectric actuator, we confirmed that the observed thermally induced change in the optical path length in ZnSe is positive (see the Supplementary Materials for details). Then, by using the $MAPbCl_3$ single crystal with the negative thermo-optic coefficient, we demonstrate the compensation of the optical phase shift occurring in ZnSe. We placed 3.9-mm-thick $MAPbCl_3$ single crystals (two single-crystal samples with same thickness) in front of each ZnSe crystal and repeated the experiment (Fig. 2D).

Mach-Zehnder interferometer for measuring the pump beam–induced phase shift

We measured the transient optical phase shift during pump beam irradiation of $MAPbCl_3$ by using a Mach-Zehnder interferometer modified from the above setup (fig. S5). The $MAPbCl_3$ single crystal was excited by 750-nm pump pulses, which were obtained from a femtosecond laser system (200 kHz; Pharos, Light Conversion) in combination with an optical parametric amplifier (OPA) (Orpheus, Light Conversion). The pulse duration was measured by the intensity autocorrelation measurement; the full width at half maximum (FWHM) of the pulse was 230 fs, assuming a Gaussian function. The spot size of the pump beam w_{pump} (defined by the radius at which the intensity falls to $1/e$ of the intensity at the center) was 68.4 μm at the sample position. The light with wavelength longer than the optical bandgap of $MAPbCl_3$ leads to two-photon absorption with a large penetration depth (see fig. S7). This induces lattice heating through relaxation of energetic carriers to the band edge and nonradiative interband recombination.

The time-resolved phase shift was measured by the pump beam–synchronized data acquisition with the modified Mach-Zehnder interferometer setup (*18*). To measure the phase shift, we used monochromatic light with an FWHM of ~5 nm obtained from the supercontinuum light source operated at 40 MHz and a wavelength-tunable band-pass filter (SuperChrome, Fianium). The monochromatic light was split into probe and reference beams by a PBS. The probe beam with horizontal polarization was coaxially aligned with the pump beam axis and normally incident on the (001) surface of the $MAPbCl_3$ single crystal. The power and spot size of the probe beam at the sample position were set to 65 μW and ~36 μm, respectively. The fluence of the probe beam was ~40 nJ/cm^2 and thus sufficiently weak to induce neither nonlinear absorption nor refractivity. By the second PBS, the probe and reference beams were combined, and the intensity of interference light was detected by using a photodetector (2001-FS-M, New Focus). A short-pass filter was placed after the second PBS to prevent the pump laser from entering the detector. An optical chopper operated at 4 Hz was used to modulate the pump beam, and a data acquisition module (NI USB-6251, National Instruments) was used to measure the transient response of the thermo-optic phase shift. By scanning the probe path length on the order of nanometer by the piezoelectric actuator, the optical phase was determined. The piezoelectric actuator also enables us to determine whether the measured phase shift is positive or negative. Using the above procedure, we measured the time-resolved phase shift of the probe beam in the $MAPbCl_3$ during photoexcitation. The measurements were performed in air at room temperature.

The polarization patterns plotted in Fig. 4 were obtained after inserting a half-wave plate in front of the photodetector. By rotating it, we detected the angular dependence of the interference between probe and reference beams for different pump powers.

PL measurements

The PL was measured under one- and two-photon excitation conditions. For one-photon excitation, we used the light with a wavelength of 360 nm. A beta-barium borate crystal was used for frequency-doubling of the 720-nm light obtained from the femtosecond laser system and the OPA. For two-photon excitation, we used the 750-nm laser light obtained from the OPA. The PL emission from the $MAPbCl_3$ single crystal was collected using a 10× near-infrared objective (Mitutoyo) and recorded by a nitrogen-cooled charge-coupled device camera equipped with a monochromator (SP 2500, Princeton Instruments). The measurements were performed in air at room temperature.

Determination of two-photon excitation coefficient

The two-photon absorption coefficient β was determined by a Z-scan method performed in air at room temperature (*31*). For this measurement, we used a 750-nm laser beam that was generated by the femtosecond laser operated at 10 kHz and the OPA. The pulse duration was characterized by the intensity autocorrelation measurement, and an FWHM of 180 fs was obtained under the assumption of a Gaussian profile. The beam was focused on a $MAPbCl_3$ single crystal with thickness L = 1.3 mm by a lens with a focal length of 200 mm. The sample was scanned along the beam axis using a motorized stage, and at each position, the transmitted light intensity was recorded using a silicon photodetector and a lock-in amplifier synchronized with the laser repetition. The beam spot size at the focal position was 30 μm. By fitting the obtained z position–dependent transmittance with equation 30 of (*31*), the product βIL under a certain peak irradiance I was determined. From the excitation irradiance dependence and L = 1.3 mm, we determined β = 2.43 cm/GW at 750 nm considering the surface reflectivity of 0.1.

SUPPLEMENTARY MATERIALS

Supplementary material for this article is available at http://advances.sciencemag.org/cgi/content/full/5/7/eaax0786/DC1

Supplementary Materials and Methods

Fig. S1. Structural characterization of a $MAPbCl_3$ single crystal.

Fig. S2. Incident angle dependence of the surface reflectivity for a p-polarized beam at 298 K.

Fig. S3. Temperature dependence of the refractive index of $MAPbCl_3$ for various wavelengths.

Fig. S4. Contributions of the thermo-optic coefficient and the linear expansion coefficient to the total optical path-length change.

Fig. S5. Schematic of the Mach-Zehnder interferometer for measuring time-resolved phase shifts during photoexcitation.

Fig. S6. PL spectra under one- and two-photon excitation.

Fig. S7. Carrier density profile under two-photon excitation.

Fig. S8. Effective temperature rise during pump laser excitation.

Fig. S9. Comparison of the thermo-optic properties of $MAPbCl_3$ and various materials.

Fig. S10. Excitation power dependence of PL under two-photon excitation.

Table S1. The list of thermo-optic coefficients and other constants of $MAPbCl_3$ and other materials.

References (*32*–*51*)

REFERENCES AND NOTES

1. M. M. Lee, J. Teuscher, T. Miyasaka, T. N. Murakami, H. J. Snaith, Efficient hybrid solar cells based on meso-superstructured organometal halide perovskites. *Science* **338**, 643–647 (2012).
2. Z.-K. Tan, R. S. Moghaddam, M. L. Lai, P. Docampo, R. Higler, F. Deschler, M. Price, A. Sadhanala, L. M. Pazos, D. Credgington, F. Hanusch, T. Bein, H. J. Snaith, R. H. Friend, Bright light-emitting diodes based on organometal halide perovskite. *Nat. Nanotechnol.* **9**, 687–692 (2014).
3. S. De Wolf, J. Holovsky, S.-J. Moon, P. Löper, B. Niesen, M. Ledinsky, F.-J. Haug, J.-H. Yum, C. Ballif, Organometallic halide perovskites: sharp optical absorption edge and its relation to photovoltaic performance. *J. Phys. Chem. Lett.* **5**, 1035–1039 (2014).
4. F. Deschler, M. Price, S. Pathak, L. E. Klintberg, D.-D. Jarausch, R. Higler, S. Hüttner, T. Leijtens, S. D. Stranks, H. J. Snaith, M. Atatüre, R. T. Phillips, R. H. Friend, High photoluminescence efficiency and optically pumped lasing in solution-processed mixed halide perovskite semiconductors. *J. Phys. Chem. Lett.* **5**, 1421–1426 (2014).
5. S. D. Stranks, G. E. Eperon, G. Grancini, C. Menelaou, M. J. P. Alcocer, T. Leijtens, L. M. Herz, A. Petrozza, H. J. Snaith, Electron-hole diffusion lengths exceeding 1 micrometer in an organometal trihalide perovskite absorber. *Science* **342**, 341–344 (2013).
6. Y. Yamada, T. Nakamura, M. Endo, A. Wakamiya, Y. Kanemitsu, Photocarrier recombination dynamics in perovskite $CH_3NH_3PbI_3$ for solar cell applications. *J. Am. Chem. Soc.* **136**, 11610–11613 (2014).
7. W. S. Yang, B.-W. Park, E. H. Jung, N. J. Jeon, Y. C. Kim, D. U. Lee, S. S. Shin, J. Seo, E. K. Kim, J. H. Noh, S. I. Seok, Iodide management in formamidinium-lead-halide-based perovskite layers for efficient solar cells. *Science* **356**, 1376–1379 (2017).
8. H. Wei, Y. Fang, P. Mulligan, W. Chuirazzi, H.-H. Fang, C. Wang, B. R. Ecker, Y. Gao, M. A. Loi, L. Cao, J. Huang, Sensitive x-ray detectors made of methylammonium lead tribromide perovskite single crystals. *Nat. Photonics* **10**, 333–339 (2016).
9. S. Yakunin, D. N. Dirin, Y. Shynkarenko, V. Morad, I. Cherniukh, O. Nazarenko, D. Kreil, T. Nauser, M. V. Kovalenko, Detection of gamma photons using solution-grown single crystals of hybrid lead halide perovskites. *Nat. Photonics* **10**, 585–589 (2016).
10. T. Chiba, Y. Hayashi, H. Ebe, K. Hoshi, J. Sato, S. Sato, Y.-J. Pu, S. Ohisa, J. Kido, Anion-exchange red perovskite quantum dots with ammonium iodine salts for highly efficient light-emitting devices. *Nat. Photonics* **12**, 681–687 (2018).
11. G. Xing, N. Mathews, S. S. Lim, N. Yantara, X. Liu, D. Sabba, M. Grätzel, S. Mhaisalkar, T. C. Sum, Low-temperature solution-processed wavelength-tunable perovskites for lasing. *Nat. Mater.* **13**, 476–480 (2014).
12. G. Ghosh, *Handbook of Thermo-Optic Coefficients of Optical Materials With Applications* (Academic Press, 1997).
13. M. Han, A. Wang, Temperature compensation of optical microresonators using a surface layer with negative thermo-optic coefficient. *Opt. Lett.* **32**, 1800–1802 (2007).
14. D. Shi, V. Adinolfi, R. Comin, M. Yuan, E. Alarousu, A. Buin, Y. Chen, S. Hoogland, A. Rothenberger, K. Katsiev, Y. Losovyj, X. Zhang, P. A. Dowben, O. F. Mohammed, E. H. Sargent, O. M. Bakr, Low trap-state density and long carrier diffusion in organolead trihalide perovskite single crystals. *Science* **347**, 519–522 (2015).
15. N. Onoda-Yamamuro, T. Matsuo, H. Suga, Dielectric study of $CH_3NH_3PbX_3$ (X = Cl, Br, I). *J. Phys. Chem. Solids* **53**, 935–939 (1992).
16. A. M. A. Leguy, P. Azarhoosh, M. I. Alonso, M. Campoy-Quiles, O. J. Weber, J. Yao, D. Bryant, M. T. Weller, J. Nelson, A. Walsh, M. Van Schilfgaarde, P. R. F. Barnes, Experimental and theoretical optical properties of methylammonium lead halide perovskites. *Nanoscale* **8**, 6317–6327 (2016).
17. G. Abbate, A. Attanasio, U. Bernini, E. Ragozzino, F. Somma, The direct determination of the temperature dependence of the refractive index of liquids and solids. *J. Phys. D. Appl. Phys.* **9**, 1945–1951 (1976).
18. H. Tahara, T. Aharen, A. Wakamiya, Y. Kanemitsu, Photorefractive effect in organic-inorganic hybrid perovskites and its application to optical phase shifter. *Adv. Opt. Mater.* **6**, 1701366 (2018).
19. T. Yamada, T. Aharen, Y. Kanemitsu, Near-band-edge optical responses of $CH_3NH_3PbCl_3$ single crystals: photon recycling of excitonic luminescence. *Phys. Rev. Lett.* **120**, 057404 (2018).
20. D. McMorrow, W. T. Lotshaw, G. A. Kenney-Wallace, Femtosecond optical Kerr studies on the origin of the nonlinear responses in simple liquids. *IEEE J. Quantum Electron.* **24**, 443–454 (1988).
21. B. R. Bennett, R. A. Soref, J. A. Del Alamo, Carrier-induced change in refractive index of InP, GaAs and InGaAsP. *IEEE J. Quantum Electron.* **26**, 113–122 (1990).
22. J. R. Whinnery, Laser measurement of optical absorption in liquids. *Acc. Chem. Res.* **7**, 225–231 (1974).
23. T. Yamada, Y. Yamada, Y. Nakaike, A. Wakamiya, Y. Kanemitsu, Photon emission and reabsorption processes in $CH_3NH_3PbBr_3$ single crystals revealed by time-resolved two-photon-excitation photoluminescence microscopy. *Phys. Rev. Appl.* **7**, 014001 (2017).
24. A. Pisoni, J. Jaćimović, O. S. Barišić, M. Spina, R. Gaál, L. Forró, E. Horváth, Ultra-low thermal conductivity in organic-inorganic hybrid perovskite $CH_3NH_3PbI_3$. *J. Phys. Chem. Lett.* **5**, 2488–2492 (2014).
25. R. Heiderhoff, T. Haeger, N. Pourdavoud, T. Hu, M. Al-Khafaji, A. Mayer, Y. Chen, H.-C. Scheer, T. Riedl, Thermal conductivity of methylammonium lead halide perovskite single crystals and thin films: a comparative study. *J. Phys. Chem. C* **121**, 28306–28311 (2017).
26. C. Shen, W. Du, Z. Wu, J. Xing, S. T. Ha, Q. Shang, W. Xu, Q. Xiong, X. Liu, Q. Zhang, Thermal conductivity of suspended single crystal $CH_3NH_3PbI_3$ platelets at room temperature. *Nanoscale* **9**, 8281–8287 (2017).
27. W. Lee, H. Li, A. B. Wong, D. Zhang, M. Lai, Y. Yu, Q. Kong, E. Lin, J. J. Urban, J. C. Grossman, P. Yang, Ultralow thermal conductivity in all-inorganic halide perovskites. *Proc. Natl. Acad. Sci. U.S.A.* **114**, 8693–8697 (2017).
28. C. Ge, M. Hu, P. Wu, Q. Tan, Z. Chen, Y. Wang, J. Shi, J. Feng, Ultralow thermal conductivity and ultrahigh thermal expansion of single-crystal organic–inorganic hybrid perovskite $CH_3NH_3PbX_3$ (X = Cl, Br, I). *J. Phys. Chem. C* **122**, 15973–15978 (2018).
29. M. Wang, S. Lin, Anisotropic and ultralow phonon thermal transport in organic-inorganic hybrid perovskites: Atomistic insights into solar cell thermal management and thermoelectric energy conversion efficiency. *Adv. Funct. Mater.* **26**, 5297–5306 (2016).
30. E. Hecht, *Optics* (Addison-Wesley, ed. 4, 2002).
31. M. Sheik-Bahae, A. A. Said, T.-H. Wei, D. J. Hagan, E. W. Van Stryland, Sensitive measurement of optical nonlinearities using a single beam. *IEEE J. Quantum Electron.* **26**, 760–769 (1990).
32. T. Handa, D. M. Tex, A. Shimazaki, A. Wakamiya, Y. Kanemitsu, Charge injection mechanism at heterointerfaces in $CH_3NH_3PbI_3$ perovskite solar cells revealed by simultaneous time-resolved photoluminescence and photocurrent measurements. *J. Phys. Chem. Lett.* **8**, 954–960 (2017).
33. N. Onoda-Yamamuro, T. Matsuo, H. Suga, Calorimetric and ir spectroscopic studies of phase transitions in methylammonium trihalogenoplumbates (II). *J. Phys. Chem. Solids* **51**, 1383–1395 (1990).
34. T. Baikie, N. S. Barrow, Y. Fang, P. J. Keenan, P. R. Slater, R. O. Piltz, M. Gutmann, S. G. Mhaisalkar, T. J. White, A combined single crystal neutron/x-ray diffraction and solid-state nuclear magnetic resonance study of the hybrid perovskites $CH_3NH_3PbX_3$ (X = I, Br and Cl). *J. Mater. Chem. A* **3**, 9298–9307 (2015).
35. S. M. Sze, K. K. Ng, *Physics of Semiconductor Devices* (John Wiley & Sons, ed. 3, 2007).
36. C. J. Glassbrenner, G. A. Slack, Thermal conductivity of silicon and germanium from 3°K to the melting point. *Phys. Rev.* **134**, A1058–A1069 (1964).
37. R. O. Carlson, G. A. Slack, S. J. Silverman, Thermal conductivity of GaAs and $GaAs_{1-x}P_x$ laser semiconductors. *J. Appl. Phys.* **36**, 505–507 (1965).
38. E. F. Steigmeier, I. Kudman, Acoustical-optical phonon scattering in Ge, Si, and III-V compounds. *Phys. Rev.* **141**, 767–774 (1966).
39. E. K. Sichel, J. I. Pankove, Thermal conductivity of GaN, 25–360 K. *J. Phys. Chem. Solids* **38**, 330 (1977).
40. G. A. Slack, Thermal conductivity of II-VI compounds and phonon scattering by Fe^{2+} impurities. *Phys. Rev. B* **6**, 3791–3800 (1972).
41. R. J. Harris, G. T. Johnston, G. A. Kepple, P. C. Krok, H. Mukai, Infrared thermooptic coefficient measurement of polycristalline ZnSe, ZnS, CdTe, CaF_2, and BaF_2, single crystal KCl, and TI-20 glass. *Appl. Opt.* **16**, 436–438 (1977).
42. H. Morkoç, S. Strite, G. B. Gao, M. E. Lin, B. Sverdlov, M. Burns, Large-band-gap SiC, III-V nitride, and II-VI ZnSe-based semiconductor device technologies. *J. Appl. Phys.* **76**, 1363–1398 (1994).
43. Y. L. Pei, Y. Liu, Electrical and thermal transport properties of Pb-based chalcogenides: PbTe, PbSe, and PbS. *J. Alloys Compd.* **514**, 40–44 (2012).
44. J. Kischkat, S. Peters, B. Gruska, M. Semtsiv, M. Chashnikova, M. Klinkmüller, O. Fedosenko, S. Machulik, A. Aleksandrova, G. Monastyrskyi, Y. Flores, W. Ted Masselink, Mid-infrared optical properties of thin films of aluminum oxide, titanium dioxide, silicon dioxide, aluminum nitride, and silicon nitride. *Appl. Opt.* **51**, 6789–6798 (2012).
45. O. Reshef, K. Shtyrkova, M. G. Moebius, S. Griesse-Nascimento, S. Spector, C. C. Evans, E. Ippen, E. Mazur, Polycrystalline anatase titanium dioxide microring resonators with negative thermo-optic coefficient. *J. Opt. Soc. Am. B* **32**, 2288–2293 (2015).
46. H. Tang, K. Prasad, R. Sanjinès, P. E. Schmid, F. Lévy, Electrical and optical properties of TiO_2 anatase thin films. *J. Appl. Phys.* **75**, 2042–2047 (1994).
47. Y. S. Touloukian, *Thermophysical Properties of Matter* (IFI Plenum, 1970).
48. G. Beadie, M. Brindza, R. A. Flynn, A. Rosenberg, J. S. Shirk, Refractive index measurements of poly(methyl methacrylate) (PMMA) from 0.4–1.6 μm. *Appl. Opt.* **54**, F139–F143 (2015).
49. D. G. Cahill, R. O. Pohl, Thermal conductivity of amorphous solids above the plateau. *Phys. Rev. B* **35**, 4067–4073 (1987).
50. J. H. Burnett, S. G. Kaplan, Measurement of the refractive index and thermo-optic coefficient of water near 193 nm. *J. Micro Nanolithogr. MEMS MOEMS* **3**, 68–72 (2004).
51. D. R. Lide, *CRC Handbook of Chemistry and Physics* (CRC Press, 2005).

Acknowledgments: We thank K. Ohara for experimental help. **Funding:** Part of this work was financially supported by JST-CREST (grant no. JPMJCR16N3) and JSPS KAKENHI (grant no. 17J09650). **Author contributions:** T.H., H.T., and Y.K. designed the study. T.H. performed the optical measurements and analyzed the data, supported by H.T. T.A. synthesized the samples. Y.K. supervised the project. All authors discussed the results and contributed to the manuscript. **Competing interests:** T.H., H.T., and Y.K. are inventors on a Japanese patent application related to this work submitted by Kyoto University (no. JP2019-028763, filed 20 February 2019). The authors declare that they have no other competing interests. **Data and materials availability:** All data needed to evaluate the conclusions in the paper are present in the paper and/or the Supplementary Materials. Additional data related to this paper may be requested from the authors.

Submitted 20 February 2019
Accepted 17 June 2019
Published 19 July 2019
10.1126/sciadv.aax0786

Citation: T. Handa, H. Tahara, T. Aharen, Y. Kanemitsu, Large negative thermo-optic coefficients of a lead halide perovskite. *Sci. Adv.* **5**, eaax0786 (2019).

ScienceAdvances

Large negative thermo-optic coefficients of a lead halide perovskite

Taketo Handa, Hirokazu Tahara, Tomoko Aharen and Yoshihiko Kanemitsu

Sci Adv **5** (7), eaax0786.
DOI: 10.1126/sciadv.aax0786